Solar Energy Materials & Solar Cells 215 (2020) 110670

Contents lists available at ScienceDirect

Solar Energy Materials and Solar Cells

journal homepage: http://www.elsevier.com/locate/solmat

Assessing mobile ions contributions to admittance spectra and current-voltage characteristics of 3D and 2D/3D perovskite solar cells

Ali Sehpar Shikoh [a], Sanghyun Paek [b], Alexander Y. Polyakov [a,**], Nikolai B. Smirnov [a], Ivan V. Shchemerov [a], Danila S. Saranin [a], Sergey I. Didenko [a], Zubair Ahmad [c,*], Farid Touati [d], Mohammad Khaja Nazeeruddin [e]

[a] Department of Semiconductor Electronics and Physics of Semiconductors, National University of Science and Technology MISiS, 4 Lenisky Ave, Moscow, 119049, Russia
[b] Department of Chemistry and Energy Engineering, Sangmyung University, Seoul, 03016, Republic of Korea
[c] Center for Advanced Materials (CAM), Qatar University, P.O.Box 2713, Doha, Qatar
[d] Department of Electrical Engineering, College of Engineering, Qatar University, P.O.Box 2713, Doha, Qatar
[e] Laboratory of Photonics and Interfaces, Institute of Chemical Sciences and Engineering, École Polytechnique Fédérale de Lausanne, CH-1015, Lausanne, Switzerland

ARTICLE INFO

Keywords:
Deep levels transient spectroscopy (DLTS)
Perovskite solar cells
2D perovskite
2D/3D perovskite

ABSTRACT

Recently, the 2D perovskite layer is employed as a capping/passivating layer in the perovskite solar cells (PSCs). The 2D perovskite layer is prepared by inserting a large-sized hydrophobic *cation* spacer into the perovskite crystal lattice. The large-sized *cation in the 2D perovskite lattice* can successfully suppress the moisture intrusion and hence improve the stability of the PSCs. However, a deep understanding of the interfacial mechanisms at the 2D/3D heterojunction and the relative contributions of the mobile ions and trapped charge carriers is still lacking. In this work, deep levels transient spectroscopy (DLTS) and reverse DLTS (RDLTS) have been performed to characterize the n-i-p structured 3D and 2D/3D PSCs. DLTS and RDLTS have been used to distinguish between the spectral contribution made by mobile ionic species, electron/hole traps, and to investigate the presence of ordinary deep electron and hole traps in the bandgap of perovskite. Besides, the PSCs have been characterized by photoinduced voltage transient spectroscopy (PIVTS) to study the decay of the open-circuit voltage (V_{OC}) under illumination. For both 3D and 2D/3D PSCs, the contribution of mobile ions was found to be dominant; however, in the case of 2D/3D samples, the intensity of the mobile ions signal was several times lower. The lower intensity can be correlated with a lower amplitude of slow tails in V_{OC} decay curves in 2D/3D solar cells as compared to 3D solar cells. The PIVTS study also endorses the 2D/3D structures as more robust than the 3D structures.

1. Introduction

Hybrid organic-inorganic perovskite materials with structural formula ABX_3 are rapidly progressing candidates for the fabrication of cost-effective solar cells. These perovskite materials possess interesting properties, such as tunable bandgaps, high absorption coefficient, large diffusion length of charge carriers, and high tolerance to defects [1]. Such advantages have made it possible to achieve high power conversion efficiency (PEC) in a very short period. Presently, the PEC of the perovskite-based solar cells has reached 25.2%. At present, the mixed cation, mixed-halide perovskite (Cs, MA, FA)Pb(I, Br)$_3$ is considered as the most promising candidate to develop stable and efficient perovskite solar cell (PSC) [2]. However, the inconsistency and the atypical hysteretic performance in the current-voltage characteristics of PSCs strongly handicaps them from their introduction into the commercial market. It has been realized that these problems are primarily related to the fact that perovskites are ionic semiconductors with a large concentration of mobile ions that contribute to the overall conductivity of these materials. Quite a few methods of studying the contribution of the movement of ions in conductivity have developed for both steady-state & dynamic conditions [3–7]. These techniques use different versions of admittance spectroscopy to reveal the role of mobile ions in low-frequency admittance and the dispersion of the dielectric constants of films with different compositions. However, high-frequency "*deep*

* Corresponding author.
** Corresponding author.
E-mail addresses: aypolyakov@gmail.com (A.Y. Polyakov), zubairtarar@qu.edu.qa (Z. Ahmad).

https://doi.org/10.1016/j.solmat.2020.110670
Received 22 April 2020; Received in revised form 30 May 2020; Accepted 16 June 2020
Available online 1 July 2020

levels transient spectroscopy" (DLTS) can extract the parameters of ion species that are involved in ionic conductivity in the perovskite materials [8–11]. Indeed, the DLTS analysis can give some new insights into the nature of the processes involved in the dark and photocurrent, photovoltage phenomena [3,6,12].

Our previous studies [9–11], revealed that the DLTS and current transient DLTS (CDLTS) measurements could discriminate the usual effects caused by electrons and holes capture and emission by deep traps in the bandgap of the perovskite materials. It argued that the electronic trapping/de-trapping processes are contributing to the transient signal and the formation of peaks in DLTS/CDLTS. Hence, we apply these procedures to analyze the defects in multi-cation PSCs with 3-dimensional (3D) perovskite layers and heterostructures between 3D multi-cation perovskite and 2-dimensional (2D) perovskites. These 2D perovskites having the general formula $R_2(A)_{n-1}B_nX_{3n+1}$ have emerged as a potential source of stability enhancement in PSCs [13] and are formed by inserting a large-sized organic cation spacer (R^+) into the perovskite lattice, thereby isolating the inorganic metal sheets and disrupting the 3D perovskite structure [14].

A few groups have recently demonstrated the strategies to fabricate a 2D/3D bi-layered perovskite heterojunctions for a highly stable device [15]. So far, the most successful method implemented (by Nazeeruddin group) [16] produced the power conversion efficiency (PCE) of 20.75%. This method involves the depositing of a bulk organic cation on a pre-formed 3D perovskite surface to induce the in-situ growth of a 2D layer, thus forming a heterostructure [15,17]. This methodology allowed the PSCs to have panchromatic absorption, excellent charge transport, reduced charge recombination and current-voltage hysteresis. Also, the 2D/3D PSCs retained 85% of initial PCE after prolonged illumination for 800 h, at 50 °C.

Thus, it was very interesting to assess the relative importance of the mobile ions contribution and charge trapping/emission via usual deep centers in the forbidden gap in such heterostructures.

2. Experimental

2.1. Fabrication of 3D and 2D/3D PSCs

The n-i-p structured PSCs studied here were prepared following the recipe described in Ref. [13]. Fig. 1(a) shows the cross-sectional SEM image of the PSCs while the Fig. 1(b) represent the schematic representation of the device in which, the electron transport layer (ETL) formed by compact TiO_2 and mesoscopic TiO_2, perovskite as absorber layer [13,18], and the hole transport layer (HTL) consisting of 2,2′,7,7′-Tetrakis[N,N-di(4-methoxyphenyl)amino]-9,9′-spirobifluorene (i.e. Spiro-OMeTAD) [13,18]. Ohmic contact to the ETL is formed by the layer of fluorine-doped tin oxide (FTO) deposited on glass, and to the HTL layer by the thermal deposition of the Au layer. The 3D samples are indeed different in only the absence of the 2D perovskite film on top of the 3D perovskite.

Fig. 2(a and b) compares the energy band diagrams of the 3D PSC and 2D/3D PSCs. With a bandgap of 1.6 eV, the absorption range of 3D ($Cs_{0.1}FA_{0.77}MA_{0.13}PbI_{0.59}Br_{0.41}$) is from 350 nm to 775 nm, with peak forming at 450 nm [13]. In contrast, the bandgap of 2D (PEA_2PbI_4) is

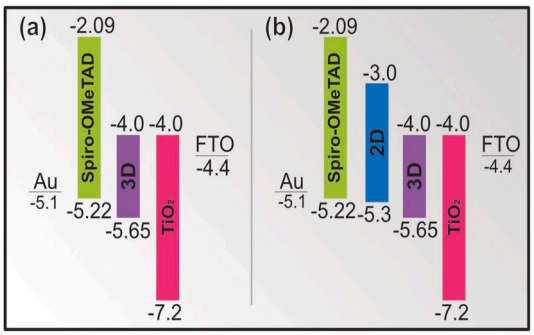

Fig. 2. Schematic representation of the energy band diagrams of the (a) 3D and (b) 2D/3D PSCs.

2.32 eV and thereby results in a narrow absorption range from 350 nm to 535 nm with a peak absorbance at 512 nm [13]. Table 1 presents the major I–V characteristics of the studied samples (two of each kind), after the fabrication, keeping the active area limited to 0.16 cm^2.

2.2. Measurement techniques

The samples were characterized using the capacitance versus frequency (C-f), capacitance versus voltage (C–V), the temperature dependence of capacitance and AC conductance at different frequencies (admittance spectra) [19], current-voltage (I–V) measurements, I–V hysteresis, and capacitance DLTS [20] techniques. The C-f and admittance measurements were done in the frequency range of 20 Hz-1 MHz. DLTS spectra were obtained in the temperature range of 100 K–350 K using the experimental setup based on E4980A LCR meter and 33500B waveform generator (KeySight Technologies, USA), as described in Ref. [20,21].

A characteristic feature of this setup is that DLTS measurements can be performed at any frequency ranging between 10 kHz and 1 MHz. During the temperature scan, full capacitance relaxation curves were measured with the chosen number of points on the decay and chosen time step between the measurements (up to 200 points could be collected with time steps of 15 ms or longer). The spectra were taken either in the normal DLTS mode (the sample kept at reverse bias and pulsed to forward bias or lower reverse bias) or in "reverse" DLTS mode

Table 1
I–V characteristics of the 3D and 2D/3D samples measured at the time of fabrication.

Sample No.	Type	V_{oc} (V)	I_{sc} (mA)	V_{mpp} (V)	I_{mpp} (mA)	FF	Efficiency %
1	3D	1.07	22.88	0.88	21.3	0.76	18.61
2	3D	1.06	22.85	0.87	21.3	0.76	18.41
15	2D/3D	1.08	23.41	0.88	21.7	0.76	19.21
16	2D/3D	1.10	23.14	0.91	21.8	0.78	19.85

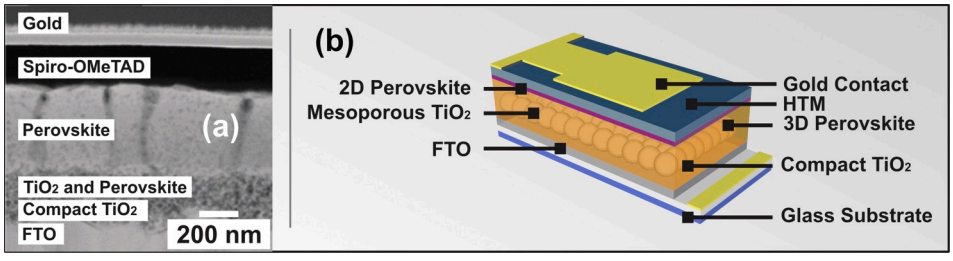

Fig. 1. (a) Cross-sectional SEM image of the PSC showing the thickness of each of the deposited layers, (b) Schematic representation of the 2D/3D device.

(RDLTS) (the sample kept at forward bias and pulsed to reverse bias) [22,23]. Obviously, for a standard semiconductor structure, de-trapping of charge carriers from electronic states in the gap, giving rise to peaks in DLTS [24] should not occur in this "reverse" DLTS mode. However, unorthodox processes, such as charging of deep traps in the barrier of high electron mobility transistor HEMT causing the change of the transistor threshold voltage [25] or movement of mobile ions causing changes in capacitance and current of a Schottky diode, as in PSCs or perovskite Schottky diodes [8–11] can result in the appearance of peaks in RDLTS spectra. The advantage of using this "reverse" DLTS technique for studying the mobile-ions-related processes in perovskites is that it is not necessary to assume that electron emission from deep states in the gap and the ion movement occur on a very different time scale, as done in Ref. [8]. Such an assumption is, in fact, very difficult to justify, whereas the presence of peaks in "reverse" DLTS in perovskite Schottky diodes is a direct indication of the involvement of mobile ions.

In addition to these measurements, the samples were characterized by a new technique known as photoinduced voltage transient spectroscopy (PIVTS). The idea here is to study the decay of the open-circuit voltage V_{OC} of PSCs after the application of illumination pulse and process the decay curves of the open-circuit voltage at different temperatures in the same two-gate technique employed in current DLTS (CDLTS) [24] or in photoinduced current transient spectroscopy (PICTS) technique [26]. The experimental setup is the same as in our PICTS measurements [27]. The difference with PICTS in our PIVTS version is that in PICTS, the current-voltage source/meter B2902A (KeySight Technologies, USA) is set to supply constant voltage and measure the transient photocurrent decay produced by the light pulse of a light-emitting diode LED also driven by the B2902A. In PICTS, these decay curves are monitored and stored during the temperature sweep with the set temperature step. The photocurrent relaxation curves at each temperature are then used to generate PICTS spectra by plotting the difference in transient current values at time windows t_1 and t_2 ($t_2 \gg t_1$) as a function of temperature. The peak in the PICTS signal occurs with the emission rate of the traps $\sim 1/t_1$ [27]. In contrast, for PIVTS, the instrument is set in a current source mode, and very low current settings (in our case 10^{-11} A) are used to monitor the voltage changes with time and process them in a similar way as in PICTS or CDLTS, but with the peak condition being with the emission time "$(t_2\text{-}t_1)/\ln(t_2/t_1)$" as in DLTS [22]. At each temperature, the relaxation curve of the V_{oc} was measured and stored, and the signal processed into the PIVTS spectra by choosing the time windows t_1& t_2, for which the PIVTS signal $\Delta V_{oc} = V_{oc}(t_1)\text{-}V_{oc}(t_2)$ was built as a function of temperature. This procedure provides a set of V_{OC} relaxation curves following the pulse of light excitation and allows to determine the temperature dependences of V_{OC} decay times in an automated way to determine then the relevant activation energies and pre-exponential factors in decay times from the temperature shift of the PIVTS peaks with changing the settings of the time windows, as in PICTS (the particulars of the method will be described in detail in a separate publication). If the relaxation time τ at the temperature corresponding to the peak of the cure is $\tau_{peak} = (t_2\text{-}t_1)/\ln(t_2/t_1)$, then, in a standard fashion, the Arrhenius plot "$\ln(1/\tau T^2)$ versus $1000/T$″ is constructed for different t_1 & t_2 settings. The slope of the Arrhenius plot yields the activation energy, and the offset provides the value of the pre-exponential factor. For conventional semiconductors solar cells, the V_{OC} relaxation times are short and determined by the charge carrier lifetime [28], hence, in our experimental conditions (decay curves digitized with time steps of 0.2 ms or longer), no peaks should be observed. However, it is well known that, in perovskites, V_{OC} values show a prominent hysteresis on the time scale of many milliseconds, and it has been suggested that these hysteresis times are related to the mobile ion rearrangements [12]. Isothermal V_{OC} measurements have directly demonstrated it at different temperatures in Ref. [29]. The method that we describe here allows us to automate these studies similar to what DLTS does for isothermal capacitance waveform analysis.

3. Results and discussion

3.1. I–V measurements

Fig. 3 shows the room temperature IV characteristics of the studied 2D/3D (red curves) and 3D PSCs measured with 530 nm light-emitting diode excitation with an optical power of 250 mW (the data in the figure are shown for sample 2D/3D#16 and 3D #2 from Table 1 for which detailed admittance spectra, DLTS characterizations are described below; for the two other samples from the table IV characteristics were very much the same, as very similar C-f, C–V characteristics at room temperature). It can be seen that in good agreement with the data of Table 1, the short circuit photocurrent I_{SC}, the V_{OC} values and the magnitude of hysteresis in I–V characteristics (measured with voltage step of 0.02 V, measurement time between successive points in voltage sweep of 20 ms, and the hold time between the sweep up and down of 5s) were similar for both samples and close to the measurements results presented in Table 1, but with I_{SC} and V_{OC} consistently slightly higher for the 2D/3D samples.

3.2. C-f, C–V and admittance spectra measurements

Fig. 4 compares room temperature, capacitance versus frequency dependences for samples with and without the 2D layer on top. The low-frequency capacitance of the structure is mainly determined by the formation of double layers at the interfaces due to the accumulation of mobile ions. The width of these layers is governed by the concentration of mobile ions that, in perovskites, is often much higher than the density of immobile centers supplying electrons and holes [2,3,12,29,30]. The usual space charge region (SCR) capacitance owing to the depletion of the near-interface region with electrons or holes is much lower. At high frequencies, when the mobile ions cannot follow the probing AC electric field in C–V measurements, the ionic capacitance simply becomes the geometrical capacitance. It does not depend on applied voltage whilst the standard electronic SCR width depends on applied voltage as predicted by the standard depletion approximation. If the SCR width at the given barrier height and given density of dopants is such that it is higher than the width of the perovskite layer, the resulting high-frequency capacitance will be equal to the geometrical capacitance of the perovskite layer. If the donors are accumulated at the back contact, then the resulting capacitance will be determined by the width of the perovskite layer up to the accumulation region [31]. For applied biases resulting in the width of the depletion layer lower than the width of the perovskite layer (in our case, this requires application of forward bias, see below) standard capacitance-voltage profiling can then be used to determine the spatial distribution of charge in the SCR region. However, one has to remember that the width of the double layer due to mobile ions still

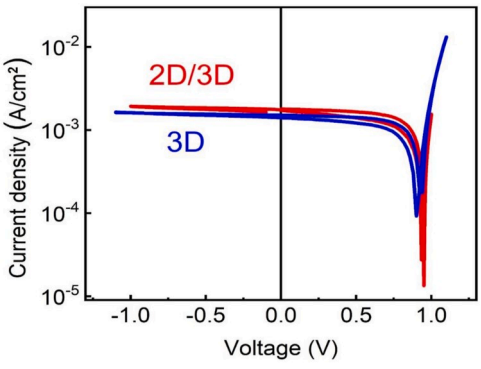

Fig. 3. I–V characteristic of 2D/3D (red line) and 3D (blue line) perovskite solar cells measured using 530 nm LED. (For interpretation of the references to color in this figure legend, the reader is referred to the Web version of this article.)

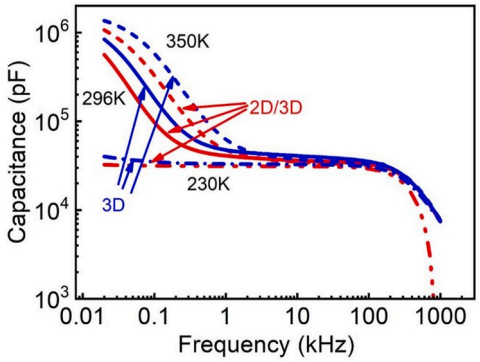

Fig. 4. C-f characteristics measured at 0 V for the 2D/3D sample (red lines) and 3D sample (blue lines) at three temperatures of 296 K (solid lines), 230 K (dash-dotted lines), and 350 K (dashed lines). (For interpretation of the references to color in this figure legend, the reader is referred to the Web version of this article.)

depends on the applied voltage and will give rise to the shift of the measured profile approximately by the effective width of the double layer at the given voltage and temperature similar to the case of a high-density layer of deep donors in standard semiconductors [32].

As seen from Fig. 4 at low frequencies, the capacitance is slightly higher for the 3D samples, presumably due to a higher concentration of mobile ions (see the discussion above). It sharply increases for both the 3D and 2D/3D samples for the high temperature of 350 K and shows a plateau in the frequency dependence indicating that the characteristic decay times associated with the movement of mobile ions become comparable with $1/(2\pi f)$ of the probing signal in capacitance measurements (f being the frequency of the signal). At low temperatures, the low-frequency capacitance strongly freezes out, indicating that the mobility of the ions is severely hampered.

At high frequencies where the mobile ions cannot follow the applied probing electric field in C–V measurements, the capacitance of the structure is, as discussed above, due to the normal "electronic" space charge region width.

When negative voltage or low positive voltage was applied at high frequencies to the top Au electrode of the structures (Fig. 1), the high-frequency capacitance was virtually constant, for positive voltages above~0.5 V the $1/C^2$ versus voltage plots in C–V characteristics were linear with the slope corresponding to the charge concentration about 10^{17} cm^{-3} and the built-in voltage close to 1.15 V for 2D/3D solar cells and 1.3 V for 3D solar cells (Fig. 5). Concentration versus depth profiles calculated from room temperature C–V characteristics are shown in Fig. 6(a) for the 2D/3D and 3D samples. The concentration is low and almost constant in the bulk of perovskite films adjacent to the HTL interface and demonstrates a charge build-up towards the ETL interface.

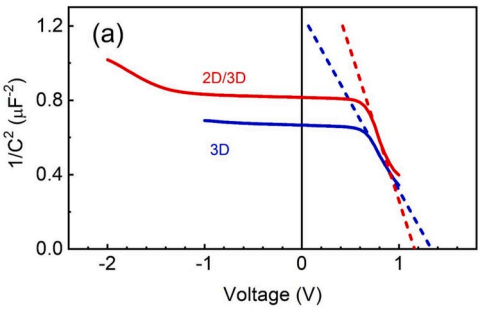

Fig. 5. Room temperature $1/C^2$ versus V dependences measured at 30 kHz for the 2D/3D sample (red line) and 3D sample (blue line). (For interpretation of the references to color in this figure legend, the reader is referred to the Web version of this article.)

The results suggest that the films are n-type and that the high-frequency plateau in C-f characteristics in Fig. 4 corresponds to the depletion of the bulk region of the films up to the accumulation region near the ETL, with the band bending determined by the built-in voltage of the HTL/perovskite heterojunction which is similar to the open-circuit voltage V_{OC} of the I–V characteristics measured under illumination. This seems to be a consequence of the impact of the double-layer contribution due to mobile ions. Even though the layer thickness cannot respond to the probing frequency, however, its width changes with applied voltage and with changing of the mobile ions density with temperature or after prolonged DLTS/admittance/PIVTS probing. For illustration, the potential distribution can be taken into account (using the Poisson equation), and it can be seen that the built-in voltage and the apparent depth of the C–V profile change with the slight variation of the applied potential. A similar phenomenon happens for a layer of deep donors near the surface that do not respond to AC probing but vary with the potential distribution and with changing of the mobile ions density with temperature.

Admittance spectra (i.e., capacitance versus temperature at different frequencies f and AC conductance G versus temperature at different frequencies) are presented in Fig. 7(a and b) for the 3D (blue lines) and 2D/3D PSCs (red lines). These spectra show that as the temperature decreases below 250 K, the high-frequency capacitance decreases and shows a step. At the same time, in high-frequency conductance, one can observe a peak. Both the temperatures of the steps in capacitance/peaks in conductance shift to higher temperatures with increasing frequency. Standard admittance spectroscopy analysis [24] gives for the energy of the centers involved in the process the energy 0.21–0.24 eV very similar for 3D and 2D/3D material. The process activation energy measured is the activation energy of electrons emission from the centers determining n-type conductivity of the films. As the emission rate becomes slower than the probing frequency in capacitance/AC conductance measurements, the occupation of the centers can no longer follow the probing frequency, and their charge does not participate in the formation of capacitance [24]. From the profiles measured at low temperature (Fig. 6(b)), it can be inferred that, once these 0.2 eV centers are frozen out, the capacitance becomes close to the geometrical capacitance of the perovskite films with the thickness close to 0.4 μm. This indicates that these centers are the main shallow donors in our perovskite films. It can be safely ruled out that the centers in question could originate somewhere in the vicinity of the ETL layers because we observed very similar centers in PSCs with very different ETL and HTL layers but with similar multi-cation perovskite layers compositions [21]. At a high temperature of 350 K, the apparent position of the interfacial peak in the concentration profile (given in Fig. 6(b)) is shifted closer to the interface, most likely because the double layer formed near the interface by mobile ions becomes thinner because of the increased density of mobile ions with temperature (see the discussion above). It can also be seen that prolonged DLTS spectra measurements with different bias/pulse settings seem to shift the apparent profile at room temperature closer to the ETL interface, presumably for the same reason: this probing tends to increase the concentration of mobile ions.

It should be noted that it is often claimed that in perovskite films of PSCs, the Fermi level is close to mid-gap so that the films are free of electrons throughout their thickness and fully depleted in capacitance measurements [1,5]. This is the basis of the dielectric constant ε of perovskites determination from the PSCs capacitance values at the high-frequency plateau [5]. Such an assumption can be quite misleading and produce a large spread in ε values that, for $MAPbX_3$ films (X standing for I or Br) have been found to strongly vary from below 10 to over 100 [5]. Moreover, it has been reported that the dielectric constant of $MAPbX_3$ strongly varies with temperature in the temperature range between ~150 K and 320 K, where the crystalline phase is tetragonal. The dielectric constant peaks at $\varepsilon = 130$ for X in the structural formula $MAPbX_3$ corresponding to I or $\varepsilon = 90$ for X standing for Br at a temperature close to 150 K at which the phase transition from tetragonal to

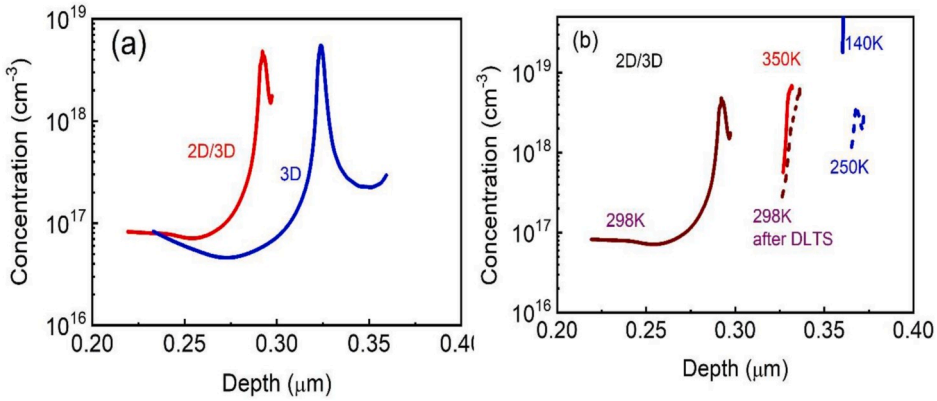

Fig. 6. Concentration versus depth profiles at room temperature for (a) 2D/3D and 3D PSCs, (b) 2D/3D PSCs at different temperatures, and before and after DLTS.

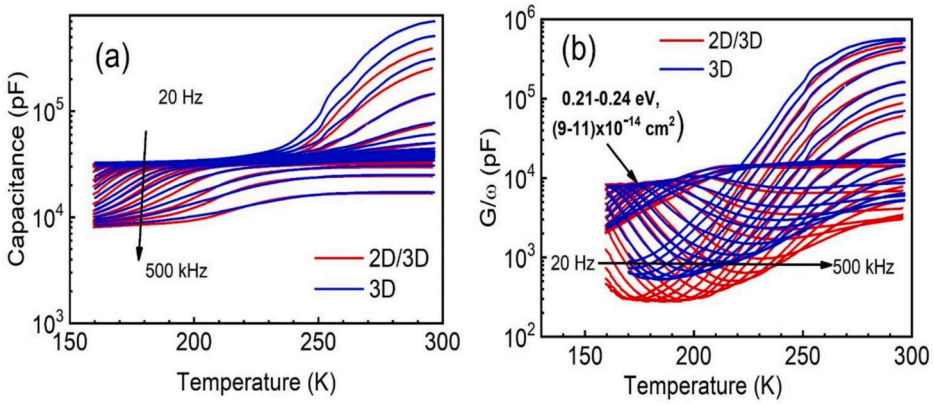

Fig. 7. (a) C-T and (b) G/ω spectra for 2D/3D and 3D PSCs, blue lines correspond to 3D and red lines to the 2D/3D sample. (For interpretation of the references to color in this figure legend, the reader is referred to the Web version of this article.)

rhombohedral phase occurs [5]. For lower temperatures, the dielectric constant in MAPbX3 is virtually constant at close to 25 for X = Br or 40 for X = I. For $CsPbI_3$, the value is not temperature-dependent and stands close to 20. At room temperature, the dielectric constant is estimated to be around 60 for X = Br or 70 for X = I [5]. Unfortunately, we have not been able to find in the literature the ε values for the perovskite layers compositions of $Cs_{0.1}FA_{0.77}MA_{0.13}PbI_{0.59}Br_{0.41}$ used in the present work. Our preliminary experiments reported in Ref. [9–11] show that for multi-cation perovskites of composition similar to the one used in the present work, the phase transition at 150 K does not occur. At the same time, it is expected that the temperature dependence of ε in multi-cation perovskites should be mostly coming from the presence of organic group in tetragonal phase of PSCs and is expected to be somewhere close to $MAPbX_3$ and fall in between the values for $MAPbI_3$ and $MAPbBr_3$. In calculating the profiles in Fig. 6 we used the ε value average between the value at room temperature and 150 K in $MAPbI_3$, ε = 80, although this choice is more or less arbitrary, and the actual values of concentrations and depths could be somewhat different. However, the profiles determined from C–V measurements at different temperatures seem quite reasonable, i.e., at low temperature where all the donors freeze out the measured space charge region width should be close to the physical thickness of the perovskite layer.

3.3. Normal and reverse DLTS measurements

We start with comparing the results of DLTS measurements for the 3D and 2D/3D samples obtained with the normal sequence of steady-state and injection pulse biases, namely the steady-state bias of −0.5 V and pulsing to 0 V for 50 ms. Fig. 8(a and b) show the spectra for time windows 30 ms/300 ms and 300 ms/3000 ms. The spectra are separated in order not to over clutter the figure). The convention in the figure is that for capacitance increasing with time after the pulse (majority carriers trap in standard DLTS [24]) the peak is positive, for capacitance decreasing with time after the pulse (minority carriers traps) the pulse is negative (the signs are as for standard charging/discharging of traps in the space charge region of a semiconductor with only electronic transitions). One can see from the outset that the data are unorthodox: we observe for both types of the samples a very prominent "minority traps" peaks at temperatures close to 270–280 K. The strangeness is in that such peaks should not be observed for purely electronic transitions because the injection pulse of 0 V should not recharge hole traps in electronic material. Also, for the 3D material, the parameters of the center responsible for the peak as deduced from standard DLTS analysis are highly unusual, i.e., the activation energy is 1 eV, and the apparent "hole" capture cross-section is 6×10^{-7} cm^2, which is unreasonable for electronic transitions. For the 2D/3D material, the activation energy is slightly lower, 0.75 eV, with the "hole" capture cross-section still unusually high, 3.1×10^{-12} cm^2. For temperatures above room temperature, "normal" electron-trap-like very broad peaks with a much lower magnitude are observed. The set of activation energies and electron capture cross sections for this set of traps is again highly unusual: for the 3D material, the activation energy is 0.35 eV, and the apparent electron capture cross-section 5×10^{-22} cm^2, for the 2D/3D material respective values are 0.2 eV, 4.8×10^{-24} cm^2. Besides, the amplitudes of the peaks change very strongly with varying the sets of the time windows in DLTS analysis and the sign of relaxations changes for longer emission times (compare the data in the figure for the time windows t1/t2 = 30 ms/300 ms (Fig. 8(a)) and 300 ms/3s (Fig. 8(b); in ordinary circumstances the

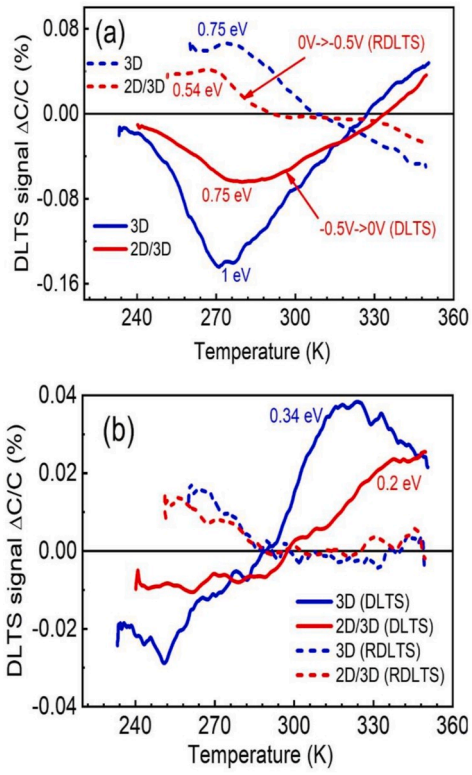

Fig. 8. (a) DLTS spectra measured for 2D/3D sample (red curves) and 3D sample (blue curves) with bias −0.5 V and pulse of 0 V (50 ms) (solid lines) and bias 0 V and pulse −0.5 V (dashed lines), time windows 30 ms/300 ms; (b) DLTS and RDLTS measured under the same biasing/pulsing conditions as in (a) for 2D/3D and 3D samples for time windows 300 ms/3000 ms, color and line type coding is same as in (a). (For interpretation of the references to color in this figure legend, the reader is referred to the Web version of this article.)

magnitudes of the peaks for different time windows settings should be the same [24]).

When the sequence of the steady-state bias and voltage pulse is changed to respectively 0 V and −0.5 V (i.e., opposite to what is done in standard DLTS, hence we call this sequence "Reverse DLTS" (RDLTS)), the picture in the spectra is mirror-like reversed (Fig. 8(a)). However, the apparent energies and apparent capture cross-sections of the peaks are measurably changed to 0.75 eV, 1.3×10^{-12} cm^2 (3D) and 0.54 eV, 2.4×10^{-18} cm^2 (2D/3D). But in both of the series, the magnitude of the peak in 2D/3D samples is several times lower than for the 3D sample (Fig. 8(a and b).

When the pulsing was done from −0.5 V to 0.3 V (normal DLTS) or vice versa (RDLTS), the asymmetry of the magnitudes of the peaks between the two types of studied samples became much less pronounced (Fig. 8(b)). The apparent activation energies did not change much for the 2D/3D samples. However, for the 3D samples, the activation energy of the main peak and the apparent capture cross-section slightly decreased.

All these features are very difficult to reconcile with the standard picture in which the capacitance relaxations are determined by the capture and emission of electrons and holes by the levels of electron and hole traps in the bandgap. If, on the other hand, the charge of the mobile ions plays a significant role in the formation of the space charge region in DLTS/RDLTS, the observed phenomena become more comprehensible. Say, in the extreme case, we neglect the charge of electrons, holes, and of immobile donors and acceptors that give rise to net electron concentration in the quasi-neutral region. Then, at reverse bias, the space charge is formed by the balance between the positively charged ion species, and negatively charged ion species and this balance gives rise to the space charge region (SCR) width W and capacitance per unit area of $\varepsilon\varepsilon_o/W$ (ε_o is, of course, the dielectric constant of vacuum). With the applied forward bias, negatively charged ions move closer and positively charged ions move further away from the Au electrode on top of HTL so that SCR decreases and capacitance increases. The return to the starting condition that causes the capacitance to decrease (in standard semiconductors this is happening when the minority carrier traps are discharged [24]) requires movement of negatively charged ions further away from the Au electrode and of the positively charged ions moving closer to the electrode. Both processes are temperature activated while the pre-exponential factor (that in DLTS on classical semiconductors is determined by the charge capture cross-section) is instead governed by the distance that the ions have to travel [8–11]. For the case of reverse DLTS, the capacitance is high at the onset, is driven to lower values by the application of reverse voltage, and then it returns to the starting condition in which the capacitance has to increase via the same process of ion movement. These extreme conditions, of course, never fully determine the capacitance and current relaxation processes, but, for low traps concentrations, can dominate in DLTS measurements. The litmus test to determine whether electronic trapping/de-trapping or the movement of mobile ions is at play is the presence of mirror-like signals in normal and reverse DLTS [9–11]. If it has been determined that the mobile ions rearrangement is at play, associated parameters such as the activation energy of the jump and the pre-exponential factor in diffusion coefficient can be calculated given that it has been established that the movement occurs via diffusion, not drift in the electric field, and the distance that the ions have to travel has been estimated [8–11]. Then, the parameters can be compared to theoretical estimates to try to pinpoint the nature of the mobile species. An additional factor to be considered is that the ionization energy of responsible defects should be low to guarantee that they are ionized irrespective of the quasi-Fermi level position. This somewhat narrows down the search when comparing the experimental values with theoretical predictions [11]. However, it should be kept in mind that the processes are complicated and are comprised of parts of decay curves for which capacitance grows with time or decreases with time, as in Fig. 8(a and b). To be able to use these measurements for quantitative assessment of the characteristics of the mobile ion, an adequate theoretical model describing the processes of ion movement and the space charge region formation is necessary.

3.4. V_{OC} kinetics studies by PIVTS

As was mentioned, the samples showed the room temperature steady-state V_{OC} values close to 1.1 V (see Table 1) and a measurable hysteresis in I–V characteristics obtained under illumination with 530 nm wavelength light-emitting diode (Fig. 3). As pointed out in several papers, the reasons for the hysteretic behavior of V_{OC} in perovskites can be closely linked to the prominent role of mobile ions and the enhancement of mobile ions formation and movement under illumination [2,12,29,30]. Our V_{OC} kinetics measurements performed using the PIVTS approach similar to that used in PICTS or CDLTS confirm these assumptions. The application of our standard suit of characterization techniques, i.e., I-V measurements (in the dark and under illumination), C-V measurements, admittance spectra measurements and DLTS spectra measurements (carried within the temperature range from 100 K to 350 K) was invasive enough to stimulate measurable changes in the ensemble of point defects in our PSCs. For example, after several DLTS measurements, the CV profiles of the samples, both 2D/3D and 3D, have measurably changed (Fig. 6(b) gives an example of how the apparent concentration profile of the 2D/3D sample at room temperature could be affected by several DLTS measurements). Thus, we compared the V_{OC} spectra collected after the whole set of characterizations with those collected for fresh samples and detected serious changes. Fig. 9(a) shows the PIVTS spectra of V_{OC} obtained for the two 3D samples, one fresh and the other studied after the application of the set of characterization techniques described above (we nickname it "tortured"). The peaks in

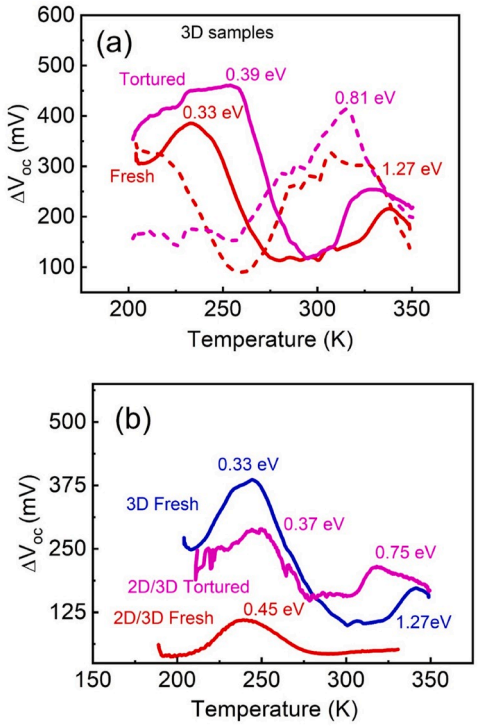

Fig. 9. (a) PIVTS spectra measured for 3D samples fresh (red line) and tortured (magenta line) with 530 nm LED excitation (optical power 250 mW, pulse length 3 s), time windows 0.8 ms/16 ms (solid lines) and 8 ms/160 ms (dashed lines); (b) spectra taken for fresh 2D/3D sample (red line), tortured 2D/3D sample (magenta line), and for fresh 3D sample (blue line, time windows 0.8 ms/16 ms. The power conversion efficiency (PCE) of the 3D and 2D/3D "fresh" samples was 18 ± 1% and 20 ± 1% while for the "tortured" devices, it was 7 ± 2% and 11 ± 2%, respectively. (For interpretation of the references to color in this figure legend, the reader is referred to the Web version of this article.)

V_{OC} PIVTS are similar to the ones observed in DLTS spectra, but that the amplitudes of the peaks are considerably higher in the "tortured" than in the fresh sample. The apparent activation energies are also measurably changed: for the fresh sample, the energies are 1.27 eV and 0.33 eV, for the tortured sample they are 0.75 eV and 0.39 eV. In Fig. 9(b), we present similar comparisons for the two 2D/3D samples, one fresh and one tortured. We also show the spectra for the fresh 3D sample to directly compare the two types of samples. It can be seen that for the 2D/3D samples "torturing" in the above-explained sense increases the magnitudes of the low-temperature peaks and shifts their respective energies from 0.45 eV to 0.37 eV while very strongly enhancing the magnitude of the high-temperature peak at 0.75 eV that is barely visible in the fresh sample. Compared to the fresh 3D sample, the fresh 2D/3D sample has a very considerably lower contribution of deep traps. Also, even the tortured 2D/3D sample looks better in that sense than the fresh 3D sample and certainly much better than the tortured 3D sample suggesting that the 2D/3D routine can produce much better robustness.

As far as the difference between two activation energies in DLTS/RDLTS and PIVTS is concerned, we can refer to the Ref. [29], where Voc relaxations were measured at different temperatures, and the equivalent circuit of the device was developed. Theoretical calculations and their comparison with the experimental results for different perovskite compositions ascribed the measured activation energies to the migration/formation energies of mobile halide ions. However, still, more studies are necessary to have deep insight into this matter.

4. Conclusions

We have revealed that by combining DLTS and RDLTS routines performed on 3D and 2D/3D samples, one can conclude that the main contribution to these spectra comes from rearrangement of the mobile ions, most likely because the density of "normal" deep traps in the bandgap of the studied PVC samples was quite low. The magnitude of the peaks is considerably higher in the 3D material than in 2D/3D material both for pulsing from −0.5 V to 0 V (normal DLTS) and from 0 V to −0.5 V (RDLTS). This new method of studying the kinetics of relaxation of V_{OC} that we named PIVTS allows us to qualitatively link the movement of ions under illumination with slow decay component in V_{OC} and with the contribution of mobile ions as detected in combined DLTS/RDLTS. The data of PIVTS suggest that the 2D/3D structures are more robust than the 3D structures and also point to the fact that the properties of the samples can be strongly affected by prolonged characterization studies involving temperature changes in a wide range and prolonged application of forward and reverse voltages. The method allows obtaining the results similar to those deduced from isothermal V_{OC} decay curves measurements [29] at different temperatures but does it more economically.

Authors contribution

All authors contributed equally.

Data availability statement

The data that support the findings of this study are available from the corresponding author upon reasonable request.

Declaration of competing interest

The authors declare that they have no known competing financial interests or personal relationships that could have appeared to influence the work reported in this paper.

CRediT authorship contribution statement

Ali Sehpar Shikoh: Methodology, Data curation, Formal analysis, Writing - original draft. **Sanghyun Paek:** Methodology. **Alexander Y. Polyakov:** Conceptualization, Project administration, Supervision, Validation, Methodology, Data curation, Formal analysis, Writing - original draft. **Nikolai B. Smirnov:** Methodology, Data curation, Formal analysis. **Ivan V. Shchemerov:** Methodology, Data curation, Formal analysis. **Danila S. Saranin:** Methodology, Data curation, Formal analysis. **Sergey I. Didenko:** Methodology, Data curation, Formal analysis. **Zubair Ahmad:** Conceptualization, Data curation, Funding acquisition, Project administration, Supervision, Validation, Writing - review & editing. **Farid Touati:** Writing - review & editing. **Mohammad Khaja Nazeeruddin:** Writing - review & editing.

Acknowledgments

This publication was made possible by NPRP Award [NPRP11S-1210-170080] from Qatar National Research Fund (a member of Qatar Foundation). The work of A.S. Shikoh at NUST MISiS was supported in part by Grant N№ K4-2018-024 under the Program to increase Competitiveness of NUST MISiS among the World Leading Scientific and Educational centers (Program funded by the Russian Ministry of Science and Education). The findings made herein are solely the responsibility of the authors.

Appendix A. Supplementary data

Supplementary data to this article can be found online at https://doi.org/10.1016/j.solmat.2020.110670.

References

[1] C. Ma, C. Leng, Y. Ji, X. Wei, K. Sun, L. Tang, et al., 2D/3D perovskite hybrids as moisture-tolerant and efficient light absorbers for solar cells, Nanoscale 8 (2016) 18309–18314.

[2] J.N. Wilson, J.M. Frost, S.K. Wallace, A. Walsh, Dielectric and ferroic properties of metal halide perovskites, Apl. Mater. 7 (2019), 010901.

[3] J. Bisquert, L. Bertoluzzi, I. Mora-Sero, G. Garcia-Belmonte, Theory of impedance and capacitance spectroscopy of solar cells with dielectric relaxation, drift-diffusion transport, and recombination, J. Phys. Chem. C 118 (2014) 18983–18991.

[4] E. Mosconi, F. De Angelis, Mobile ions in organohalide perovskites: interplay of electronic structure and dynamics, ACS Energy Lett. 1 (2016) 182–188.

[5] S. Govinda, B.P. Kore, M. Bokdam, P. Mahale, A. Kumar, S. Pal, et al., Behavior of methylammonium dipoles in MAPbX3 (X= Br and I), J. Phys. Chem. Lett. 8 (2017) 4113–4121.

[6] X. Deng, X. Wen, J. Zheng, T. Young, C.F.J. Lau, J. Kim, et al., Dynamic study of the light soaking effect on perovskite solar cells by in-situ photoluminescence microscopy, Nano Energy 46 (2018) 356–364.

[7] D.A. Jacobs, H. Shen, F. Pfeffer, J. Peng, T.P. White, F.J. Beck, et al., The two faces of capacitance: new interpretations for electrical impedance measurements of perovskite solar cells and their relation to hysteresis, J. Appl. Phys. 124 (2018) 225702.

[8] M.H. Futscher, J.M. Lee, L. McGovern, L.A. Muscarella, T. Wang, M.I. Haider, et al., Quantification of ion migration in CH 3 NH 3 PbI 3 perovskite solar cells by transient capacitance measurements, Mater. Horiz. 6 (2019) 1497–1503.

[9] N.S. Alexander Polyakov, Ivan Shcemerov Shchemerov, Danila Saranin, Anna Pozniak, Ali Sehpar Shikoh, Sergey Didenko, Denis Kuznetsov, Antonio Agresti, Sara Pescetelli, Fabio Matteocci, Aldo Di Carlo, Admittance spectroscopy and DLTS measurements on multication mesoscopic perovskite solar cells, in: International Conference on Hybrid and Organic Photovoltaics (HOPV19), Roma, Italy, 2019.

[10] A.Y.P.A.S. Shikoh, N.B. Smirnov, I.V. Shchemerov, D.S. Saranin, A. Pazniak, S. I. Didenko, D.V. Kuznetsov, A. Agresti, S. Pescetelli, A. Di Carlo, Discriminating contributions of ions and deep traps of perovskite films using low frequency admittance spectroscopy and reverse DLTS/CDLTS spectra measurements on Au/perovskite Schottky diodes, in: 5th International Conference on Advanced Electromaterials, Jeju, South Korea, 2019.

[11] A. Sehpar Shikoh, A.Y. Polyakov, N.B. Smirnov, I.V. Shchemerov, D.S. Saranin, S. I. Didenko, et al., Ion dynamics in single and multication perovskite, ACS Appl. Energy Mater. xx (2020) xx.

[12] S.A. Weber, I.M. Hermes, S.-H. Turren-Cruz, C. Gort, V.W. Bergmann, L. Gilson, et al., How the formation of interfacial charge causes hysteresis in perovskite solar cells, Energy Environ. Sci. 11 (2018) 2404–2413.

[13] K.T. Cho, G. Grancini, Y. Lee, E. Oveisi, J. Ryu, O. Almora, et al., Selective growth of layered perovskites for stable and efficient photovoltaics, Energy Environ. Sci. 11 (2018) 952–959.

[14] R. Yang, R. Li, Y. Cao, Y. Wei, Y. Miao, W.L. Tan, et al., Oriented quasi-2D perovskites for high performance optoelectronic devices, Adv. Mater. 30 (2018), e1804771.

[15] K. Lee, J. Kim, H. Yu, J.W. Lee, C.-M. Yoon, S.K. Kim, et al., A highly stable and efficient carbon electrode-based perovskite solar cell achieved via interfacial growth of 2D PEA 2 PbI 4 perovskite, J. Mater. Chem. 6 (2018) 24560–24568.

[16] G. Grancini, C. Roldan-Carmona, I. Zimmermann, E. Mosconi, X. Lee, D. Martineau, et al., One-Year stable perovskite solar cells by 2D/3D interface engineering, Nat. Commun. 8 (2017) 15684.

[17] T. Niu, J. Lu, X. Jia, Z. Xu, M.-C. Tang, D. Barrit, et al., Interfacial engineering at the 2D/3D heterojunction for high-performance perovskite solar cells, Nano Lett. 19 (2019) 7181–7190.

[18] K.T. Cho, S. Paek, G. Grancini, C. Roldán-Carmona, P. Gao, Y. Lee, et al., Highly efficient perovskite solar cells with a compositionally engineered perovskite/hole transporting material interface, Energy Environ. Sci. 10 (2017) 621–627.

[19] A. Polyakov, N. Smirnov, A. Govorkov, E. Kozhukhova, S. Pearton, F. Ren, et al., Admittance spectra studies of quantum well states in AlGaN/AlN/GaN heterojunctions, ECS J. Solid State Sci. Technol. 1 (2012) P152.

[20] A.Y. Polyakov, N.B. Smirnov, I.-H. Lee, S.J. Pearton, Deep level transient spectroscopy in III-Nitrides: decreasing the effects of series resistance, J. Vac. Sci. Technol., B Nanotechnol. Microelectron.: Mater. Process. Meas. Phenom. 33 (2015), 061203.

[21] A. Polyakov, N. Smirnov, I. Shchemerov, D. Saranin, T. Le, S. Didenko, et al., Trap states in multication mesoscopic perovskite solar cells: a deep levels transient spectroscopy investigation, Appl. Phys. Lett. 113 (2018) 263501.

[22] A. Polyakov, N. Smirnov, A. Govorkov, A. Markov, T. Yugova, A. Dabiran, et al., Electrical and structural properties of AlN/GaN and AlGaN/GaN heterojunctions, J. Appl. Phys. 104 (2008), 053702.

[23] A.Y. Polyakov, N. Smirnov, A. Govorkov, E. Kozhukhova, S.J. Pearton, F. Ren, et al., Deep centers and persistent photocapacitance in AlGaN/GaN high electron mobility transistor structures grown on Si substrates, J. Vac. Sci. Technol., B Nanotechnol. Microelectron.: Mater. Process. Meas. Phenom. 31 (2013), 011211.

[24] D.K. Schroder, Semiconductor Material and Device Characterization, third ed. ed., John Wiley & Sons, Hoboken, New Jersey, USA, 2015.

[25] A.Y. Polyakov, N.B. Smirnov, A. Govorkov, E. Kozhukhova, S.J. Pearton, F. Ren, et al., Metastable centers in AlGaN/AlN/GaN heterostructures, J. Vac. Sci. Technol., B Nanotechnol. Microelectron.: Mater. Process. Meas. Phenom. 30 (2012), 041209.

[26] M. Tapiero, N. Benjelloun, J. Zielinger, S. El Hamd, C. Noguet, Photoinduced current transient spectroscopy in high-resistivity bulk materials: instrumentation and methodology, J. Appl. Phys. 64 (1988) 4006–4012.

[27] A. Polyakov, N. Smirnov, I. Shchemerov, D. Gogova, S. Tarelkin, I.-H. Lee, et al., Electrical properties of bulk, non-polar, semi-insulating M-GaN grown by the ammonothermal method, ECS J. Solid State Sci. Technol. 7 (2018) P260–P265.

[28] H. Zhang, X. Qiao, Y. Shen, M. Wang, Effect of temperature on the efficiency of organometallic perovskite solar cells, J. Energy Chem. 24 (2015) 729–735.

[29] F. Ebadi, M. Aryanpour, R. Mohammadpour, N. Taghavinia, Coupled ionic-electronic equivalent circuit to describe asymmetric rise and decay of photovoltage profile in perovskite solar cells, Sci. Rep. 9 (2019) 1–9.

[30] D. Walter, A. Fell, Y. Wu, T. Duong, C. Barugkin, N. Wu, et al., Transient photovoltage in perovskite solar cells: interaction of trap-mediated recombination and migration of multiple ionic species, J. Phys. Chem. C 122 (2018) 11270–11281.

[31] A. Halverson, Comparison of capacitance spectroscopy for PV semiconductors, in: J.V. Li, G. Ferrari (Eds.), Capacitance Spectroscopy of Semiconductors, Jenny Stanford Publishing, Singapore, 2018, p. 221.

[32] J. Lauwaert, S. Khelifi, Deep-level transient spectroscopy, in: J.V. Li, G. Ferrari (Eds.), Capacitance Spectroscopy of Semiconductors, Jenny Stanford Publishing, Singapore, 2018, p. 61.